Aerogel RICH Counter at the Belle II Detector

I. Adachi[a], N. Akopov[b], D. Augueste[c], J. Bonis[c], L. Burmistrov[c,1], R. Dolenec[e,d], G. Ghevondyan[b], R. Giordano[f], A. Hvala[d], T. Iijima[k], S. Iwata[h], H. Kakuno[h], G. Karyan[b], H. Kawai[i], T. Kohriki[a], T. Konno[l], S. Korpar[g,d,*], P. Križan[e,d], Y. Lai[a], A. Lozar[d], M. Mrvar[d,2], G. Nazaryan[b], S. Nishida[a,*], S. Ogawa[j], R. Pestotnik[d], I. Prudiiev[d], L. Šantelj[e,d], A. Seljak[d], L. Senekovič[d], M. Shoji[a], K. Špenko[d], T. Sumiyoshi[h], M. Tabata[i], K. Uno[a], T. Yonenaga[h], Y. Yusa[m]

[a]*Institute of Particle and Nuclear Studies KEK Tsukuba Japan*
[b]*Alikhanyan National Science Laboratory, Yerevan 0036, Armenia*
[c]*Universite Paris-Saclay, CNRS/IN2P3, IJCLab, 91405 Orsay, France*
[d]*Jožef Stefan Institute, Ljubljana, Slovenia*
[e]*Faculty of Mathematics and Physics, University of Ljubljana, Ljubljana, Slovenia*
[f]*University of Naples "Federico II" and INFN, Naples, Italy*
[g]*Faculty of Chemistry and Chemical Technology, University of Maribor, Maribor, Slovenia*
[h]*Institute of Particle and Nuclear Studies, KEK, Tsukuba, Japan*
[i]*Chiba University, Chiba, Japan*
[j]*Toho Metropolitan University, Funabashi, Japan*
[k]*Nagoya University, Nagoya, Japan*
[l]*Kitasato University, Sagamihara, Japan*
[m]*Niigata University, Yusa, Japan*

Abstract

We report on the construction, operation, and performance of an innovative proximity-focusing Ring Imaging Cherenkov counter with a multi-layer focusing aerogel radiator used for the forward region of the Belle II spectrometer at the SuperKEKB e^+e^- collider. The device provides good discrimination among charged pions, kaons, and protons in the full kinematic region of the experiment, from 0.5 GeV/c to 4 GeV/c. To date, the detector has been used to record and analyze almost 600 fb^{-1} of Belle II data.

Keywords: RICH, aerogel radiator, HAPD, Belle II, ARICH

1. Introduction

The Belle II experiment in Tsukuba, Japan, is dedicated to precision measurements of rare decays of B and D mesons and τ leptons. After an excellent operation of the Belle spectrometer from 1999 to 2010 and after numerous physics analyses, the search for deviations from the Standard Model of elementary particles in very rare decay channels required an increase of the data sample by two orders of magnitude. To record such a data sample, a major upgrade of the KEKB e^+e^- collider was carried out. The new SuperKEKB accelerator was designed to operate at a 30 times higher event rate than its predecessor and is expected to collect an integrated luminosity of 50 ab^{-1} [1]. The higher event rates and correspondingly higher backgrounds required a significant upgrade of the Belle spectrometer, leaving only the mechanical structure and the 1.5 T solenoid magnet unchanged [2, 3, 4].

To achieve its physics goals, a highly efficient separation between kaons and pions in the momentum range of up to 4 GeV/c is carried out with two dedicated subsystems, both based on the detection of Cherenkov photons. While identification in the barrel region of the spectrometer is covered by a Time-of-Propagation counter (TOP) [5], the Aerogel Ring Imaging Cherenkov (ARICH) detector, as described in this paper, has been designed to separate kaons from pions over most of their momentum spectrum in the forward (end-cap) part of the Belle II spectrometer (Fig. 1).

ARICH is a proximity focusing Ring Imaging Cherenkov (RICH) counter (Fig. 2) with the following components: a *radiator* where Cherenkov photons are produced by charged particles, an *expansion volume* to allow Cherenkov photons to form rings on the photon detector surface, an array of *position sensitive photon detectors* that is capable of detecting single photons in a high magnetic field with high efficiency and with good resolution in two dimensions, and a *read-out system* for the photon detector.

The paper is structured as follows. We will first review the design choices and present all components: the aerogel radiator, the photo sensors, the read-out electronics, the mechanical structure, and the services. We will discuss the simulation and reconstruction methods and finally review the performance of the detector during the operation with electron and positron beams.

*Corresponding authors
Email addresses: samo.korpar@ijs.si (S. Korpar), shohei.nishida@kek.jp (S. Nishida)
[1]Present address: Université de Genève, Geneva, Switzerland.
[2]Present address: HEPhy, Vienna, Austria.

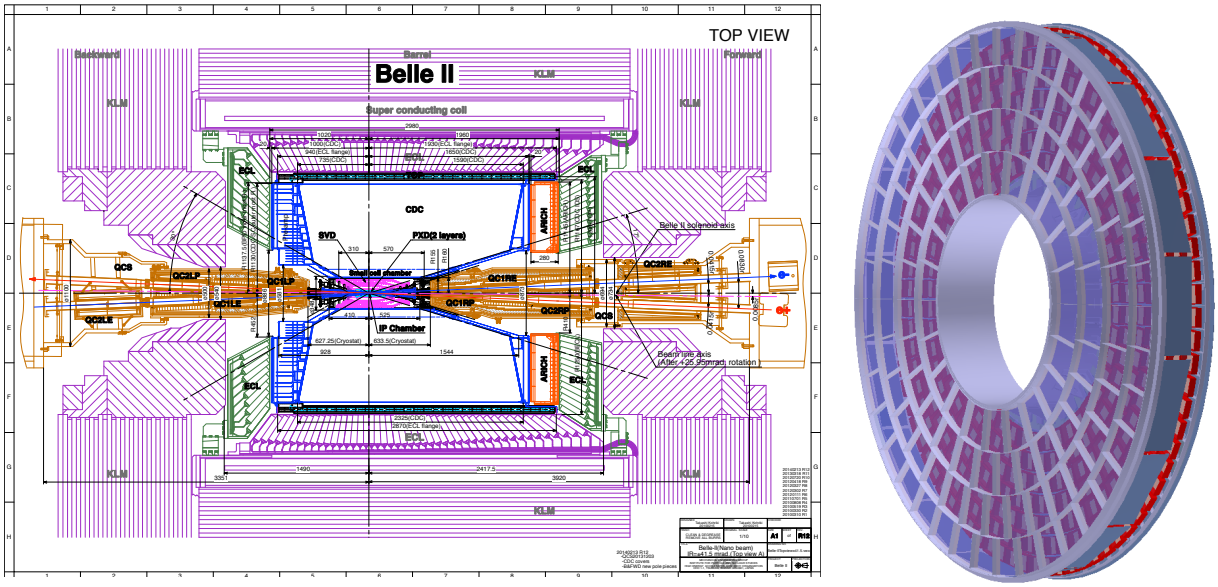

Figure 1: The Belle II spectrometer (left) and the geometry of the ARICH detector (right) with its main components, aerogel radiator (depicted in blue) and photo-sensors (in dark red).

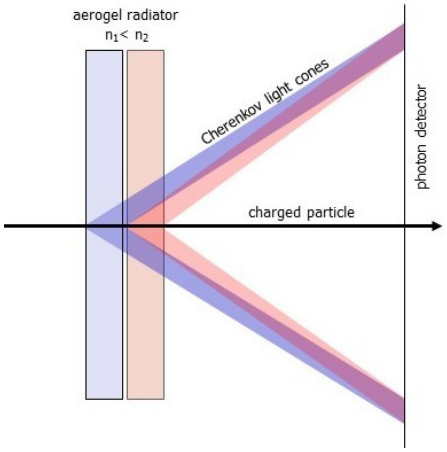

Figure 2: Proximity focusing RICH with a dual radiator in the focusing configuration.

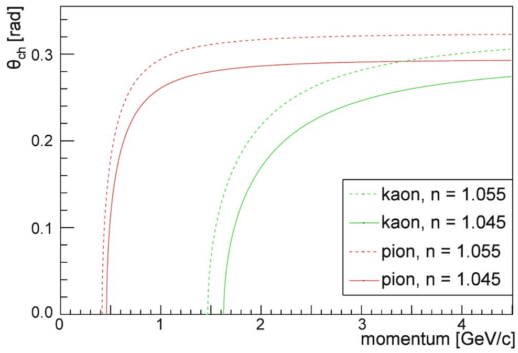

Figure 3: Cherenkov angle for pions and kaons for two refractive indices of the Cherenkov radiator, 1.045 and 1.055.

2. Design choices

The following criteria govern the design choices. The kinematic range of the experiment (pion and kaon momenta from 0.5 GeV/c to 4 GeV/c) necessitates the use of aerogel with refractive index around 1.05 as the radiator medium (Fig. 3). To achieve the necessary performance, enough photons (about 10) have to be detected for each ring image, at least for one of the particle species. This requirement fixes the length of the aerogel radiator to several centimeters. The required resolution in the measurement of the Cherenkov angle for a 3σ pion-kaon separation with such a detector ($\approx$ 7 mrad) is achievable only if the expansion gap is at about 20 cm and the photon detector granularity is a few millimeters.

A proof-of-principle counter prototype showed excellent performance both in on-the-bench and beam tests [6]. However, two significant issues remained: the need to increase the number of detected Cherenkov photons and the development of a detector for single photons that would reliably work in the 1.5 T magnetic field of the Belle II spectrometer. Both problems were solved satisfactorily, as discussed below.

The key parameter in the performance of a RICH counter is the Cherenkov angle resolution per charged particle $\sigma_{\text{track}} = \sigma_\theta / \sqrt{N}$. With a longer radiator, the number of detected photons increases, but the single photon resolution degrades in a proximity focusing RICH because of the emission point uncertainty. As it turns out, for the given available space in the spectrometer, the optimal thickness is around 20 mm [6, 7]. However, in this case, the number of detected photons is too small. This problem can be solved if a proximity focusing RICH with a

non-homogeneous radiator is employed [7, 8, 9, 10]. By appropriately choosing the refractive indices of consecutive aerogel radiator layers, one may achieve overlapping of the corresponding Cherenkov rings on the photon detector (Fig. 2) [7, 8]. This represents a sort of focusing of the photons within the radiator; it eliminates or considerably reduces the spread due to the emission point uncertainty. Note that such tuning of refractive indices for individual layers is only possible with aerogel, which may be produced with any desired refractive index in the range 1.01-1.2 [11]. In Fig. 4, we compare beam test data for

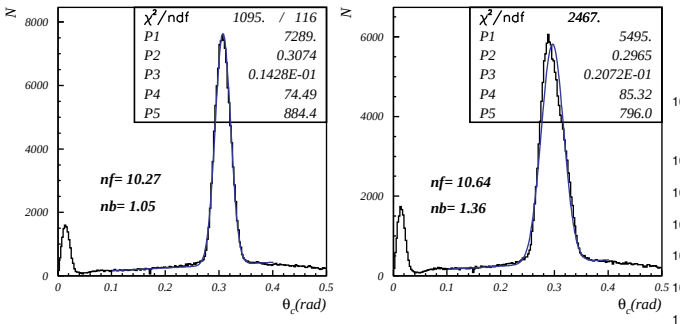

Figure 4: Proximity focusing RICH, proof of principle in a beam test: the accumulated distribution of Cherenkov photon hits depending on the corresponding Cherenkov angle for a 4 cm homogeneous radiator (right) and for a focusing configuration with two 2 cm thick layers with $n_1 = 1.046$, $n_2 = 1.056$ (left) [12].

two 4 cm thick radiators; one with aerogel tiles of equal refractive index (n = 1.046), the other with the focusing arrangement ($n_1 = 1.046, n_2 = 1.056$) [12]. The improvement is clearly visible; the single photon resolution $\sigma_\theta = 14.3$ mrad for the dual radiator is considerably better than the corresponding value for the single refractive index radiator case ($\sigma_\theta = 20.7$ mrad), while the number of detected photons is the same in both cases [3].

The second open issue, the development of a sensor of single photons for operation in the magnetic field of 1.5 T and in an environment with an expected radiation load with a neutron fluence of about 10^{11} 1 MeV n_{eq} cm^{-2} per year, has also been solved adequately, as will be reported in the following sections. The hybrid avalanche photo-detector (HAPD, by Hamamatsu Photonics) of the proximity focusing type was selected as the Cherenkov light sensor. As alternatives, two further sensors were successfully studied: a multi-channel microchannel plate photomultiplier tube (MCP-PMT) [13, 14, 15, 16] and a silicon photomultiplier (SiPM) based photon sensor [17, 18].

Another constraint on the detector design comes from the need to mitigate the loss of photons at the side walls of the ARICH vessel, as illustrated in Fig. 5. Planar mirrors are used to reflect the photons back into the sensitive area.

[3] An alternative geometry was also studied with a reversed order of the two aerogel tiles that would produce two separate rings [7]; while interesting, this de-focusing configuration was not further pursued because, with two separate rings that cover a larger area of the photon detector than a single ring, the background level would increase and could therefore deteriorate the particle identification performance.

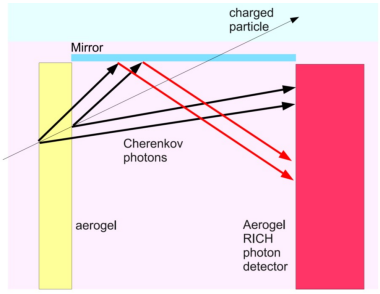

Figure 5: Recovery of photons emitted at the outer edge of the ARICH detector acceptance: planar mirrors on the side wall of the ARICH vessel.

3. Aerogel

The radiator plane comprises two layers of wedge-shaped hydrophobic aerogel tiles with nominal refractive indices of $n = 1.045$ in the first and $n = 1.055$ in the second layer. As discussed in Sec. 2, they are chosen in such a way that Cherenkov rings from the first and second layers overlap on the detector plane (Fig. 2) for the relevant kinematic range and a wide range of incidence angles [8].

The aerogel tiles, in total 124 for each refractive index, have been fabricated with the super-critical drying method [19] at the Japan Fine Ceramics Center. As shown in Fig. 6, the radiator system is segmented into four rings, each equipped with a separate type of wedge-shaped tiles. The tiles have been cut out of square-shaped $180 \times 180 \times 20$ mm^3 pieces of aerogel using a water-jet cutting device.

To obtain a good PID performance, the aerogel tiles should not be physically damaged (with no cracks or chips) and should have good transparency. Figures 7, 8, and 9 show the distributions of the refractive indices and transmission lengths of the aerogel tiles from the mass production.

The refractive index of the tiles was controlled with appropriate precision so that the difference in the refractive index of the downstream and upstream tile pairs, $n_2 - n_1 = 0.0098 \pm 0.0002$ (Fig. 9), is well within the optimal interval [8].

4. Photon detector - HAPD

As the sensor for single Cherenkov photons, a hybrid avalanche photodetector (HAPD) (Fig. 10) is used, where photoelectrons are accelerated in a static electric field and are detected with a segmented avalanche photodiode (APD). The photon detector plane is covered with 420 HAPDs, arranged in seven concentric rings as shown in Fig. 6.

The HAPD employed in the Belle II ARICH detector has been developed in collaboration with Hamamatsu Photonics [22, 21, 20]. It has outer dimensions of $7.3 \times 7.3 \times 2.0$ cm^3, a bi-alkali photo-cathode on the inner side of the quartz window, and four pixelated avalanche photo-diodes (APDs) at the bottom of the tube, each with 36 5×5 mm^2 channels (Fig. 10). The pixel size is 4.9×4.9 mm^2, and the gap between pixels is 0.2 mm within the APD; APDs are separated by 1.5 mm. The active area is about 65% of the HAPD package size. The total

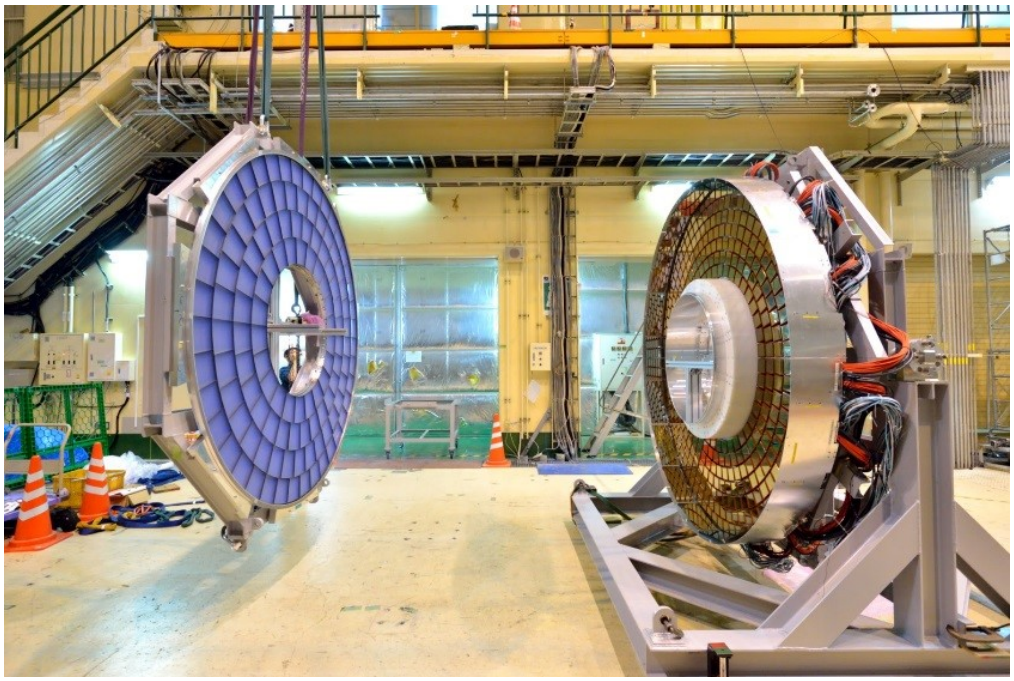

Figure 6: Two halves of the ARICH detector: radiator plane covered with two layers of aerogel tiles (left), photon detector plane covered with 420 HAPDs and planar mirrors mounted on the side wall (right), before the two were joined to form a single vessel.

gain of about 3×10^4, comprised of the bombardment gain and the gain in the APD, is provided by the high voltage of 6 kV applied to the tube; the bias voltage applied to the APD is such that the gain in the APD amounts to 30. The quantum efficiency (Q.E.) of the photo-cathode at 400 nm is between $\approx$ 25% and $\approx$ 40% as can be seen in Fig. 11. The photo-electron detection efficiency is around 90%.

Following a set of radiation tolerance tests [23] with neutrons and gamma rays, the sensor production was optimized (thicknesses of p and p^+ layers, additional intermediate electrode). The final version of tested samples retained the required performance at the neutron fluence of 10^{12} 1 MeV n_{eq} cm^{-2}, expected in the lifetime of the experiment. Another optimization of the sensor production (getter re-activation in the vacuum tube) was carried out to mitigate instabilities in the form of discharges when operated in the 1.5 T magnetic field [24].

The high-voltage system for the HAPDs consists of 8 CAEN SY4527 crates, 45 CAEN A7042P 48-channel 500 V common floating return boards, supplying four bias voltages and one guard voltage for each of the 420 HAPDs, and 28 CAEN A1590 - AG590 16-channel 9 kV boards supplying 420 high voltages.

5. Readout Electronics

A total of 60480 readout channels are needed to equip 420 HAPDs, with a single bit of on/off hit information for each channel. As shown in Fig. 14, a front-end board (FEB) with 4 ASICs and an FPGA (Xilinx Spartan 6, XC6SLX45-2FGG484) is attached to each HAPD. The ASIC, called SA03, was developed in the X-FAB 0.35 μm process technology in collaboration with Japan Aerospace Exploration Agency (JAXA). It has a preamplifier with a variable gain between 17 mV/fC and 56 mV/fC, a shaper with a shaping time that can be set to 170, 210, 240, and 350 ns, and a discriminator [25]. Each ASIC has 36 channels and processes the analog signals from the APD chip of the HAPD. A common threshold voltage is applied to the discriminator of the ASIC, while the baseline voltage of each channel can be adjusted so that, effectively, the threshold of each channel can be set independently.

The digital signals, output from ASICs, are processed in the FPGA [25, 26], and sent to the back-end electronics board ('merger') located behind the front-end boards using parallel cables. The merger board, equipped with another FPGA (Xilinx Virtex 5, XC5VLX50T-1FFG665C), collects data from 5 to 6 front-end boards, performs zero-suppression to reduce data size, and transfers them to the central DAQ through the Belle2Link [27]. The slow control, such as the read and write of the parameters in the ASICs, FEBs, and in the merger, is realized through the Belle2Link. The merger also receives the first level (L1) trigger signal and distributes it to the front-end boards.

The front-end readout board and the merger board are designed to withstand a neutron fluence equivalent to 1 MeV of 10^{12} n/cm^2 and a gamma radiation dose of 100 Gy over the expected lifetime of the Belle II spectrometer.

The low-voltage supply system for the read-out electronics is comprised of two Wiener MPOD systems and 12 low-voltage Wiener MPV8008LI modules (with 8 channels, output voltage 0 V-8 V at 5A, 40 W per channel, floating with < 2 mVp-p ripple). These modules provide supply voltages of +3.8 V, +2 V, and -2 V to the 420 front-end cards and +1.5 V and +3.8 V to

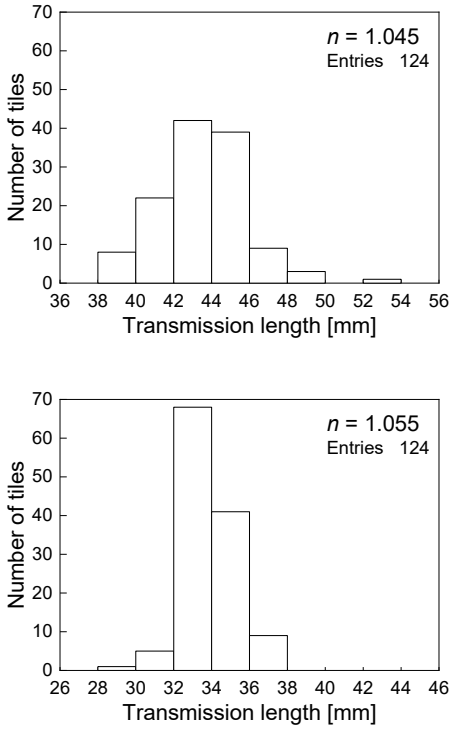

Figure 7: Aerogel properties of the installed tiles: the distribution over the transmission length at 400 nm for the upstream (top) and downstream tiles (bottom).

the 72 merger cards. From the three supply voltages at a front-end board, a reference voltage of 1.25 V is generated by a diode, while other operating voltages are provided by low dropout regulators (LDOs). An analog-to-digital converter (ADC) digitizes the various internal voltage levels, selectable via a multiplexer. The discriminator threshold level is adjusted using a digital potentiometer. Additionally, the board is equipped with an internal 42 MHz oscillator to clock the FPGA; an external clock is used during data taking operation with the Belle II detector.

The hit information from the HAPD sensors is read out in four adjacent time intervals. In the standard configuration, one timing bin corresponds to 125.6 ns so that the time window for the readout is 502.4 ns. The middle two timing bins are adjusted to the correct timing with respect to the L1 trigger, and the two side bins are used to estimate the background level on an event-by-event basis (see also Sec. 9.2).

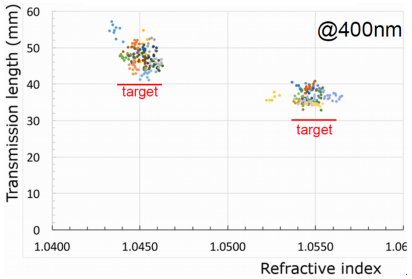

Figure 8: Aerogel properties of the installed tiles. The horizontal axis shows the refractive index, while the vertical axis shows the transmission length at 400 nm. Colours indicate different production batches.

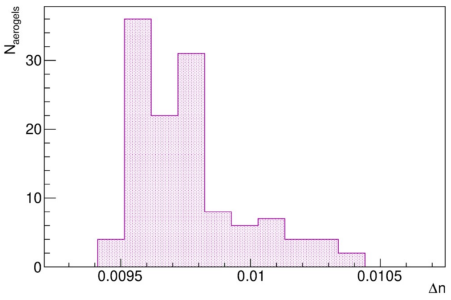

Figure 9: Aerogel properties of the installed tiles: the difference in refractive index between downstream and upstream tiles.

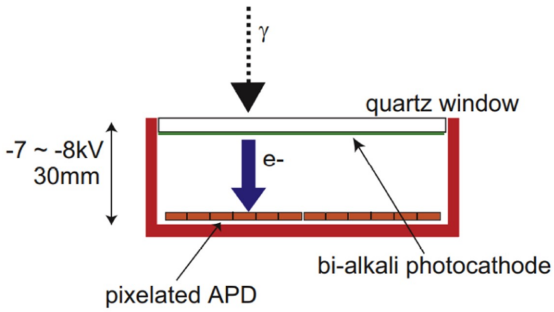

Figure 10: HAPD single-photon sensor; top: the principle of operation [20, 21], bottom: a photograph of the sensor.

5.1. *Firmware Design*

The firmware system integrates a 64-bit instruction decoder, a data sender, a command receiver, and a response sender. Instructions are received via an unidirectional asynchronous Serial Peripheral Interface (SPI). The response to each command is returned encoded in a response word through a separate, dedicated one-way SPI channel. A trigger signal activates the data encoder, which then transmits data to the merger board via another one-way SPI.

Each hardware peripheral device is managed by a driver, which is activated by the instruction decoder. Additionally, a data register controls the mode of operation, sampling rates, and encoder frequencies. The unique FPGA device identifier (DNA) is used to identify the board.

To mitigate the impact of single-event upsets (SEUs) at the FPGAs of the FEBs, a scrubber of the configuration data of the

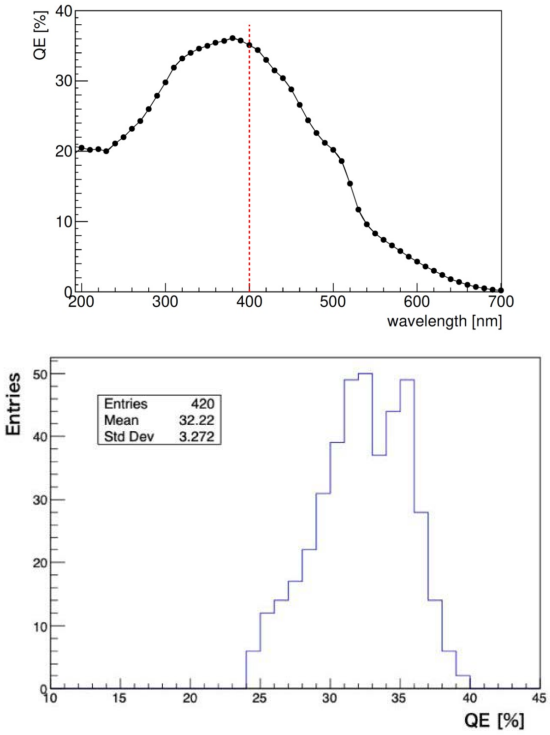

Figure 11: HAPD single-photon sensor; top: quantum efficiency of a typical sensor as a function of wavelength, the red line indicating the reference wavelength of 400 nm; bottom: quantum efficiency at 400 nm for all installed HAPDs.

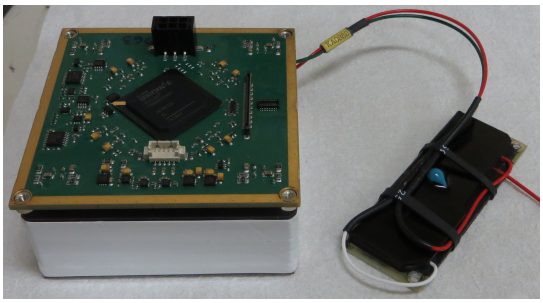

Figure 13: HAPD read-out and high voltage supply: the front-end board on top of the HAPD and the high voltage supply board; when installed in the detector, the high voltage supply board gets mounted above the front-end board.

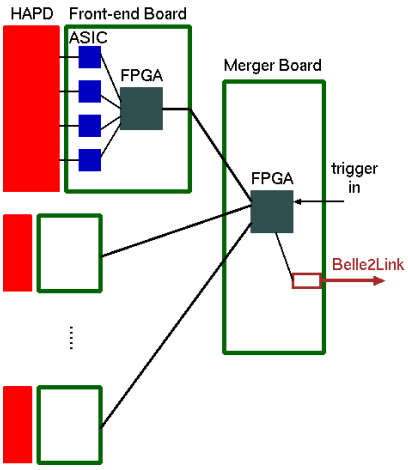

Figure 14: Readout electronics for ARICH: schematics.

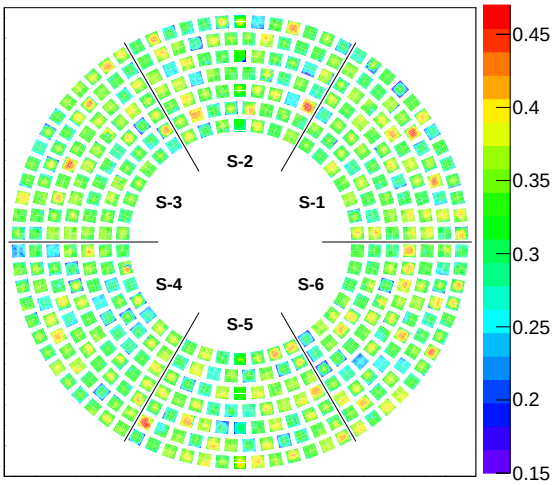

Figure 12: ARICH photon detector plane: quantum efficiency at 400 nm as a function of the photon impact coordinate.

FEBs is implemented in the firmware of the merger [29]. The scrubber monitors the SEUs at FPGAs of FEBs and corrects them by a partial reconfiguration.

6. Mechanical structure and services

The ARICH detector components are mounted inside a donut-shaped vessel as shown in Fig. 6. The vessel is comprised of two halves, one housing the aerogel radiator system, and the other the photon detectors with the read-out electronics.

On the photon detector side, the HAPDs and the associated read-out electronics are mounted on an aluminum support structure, comprised of six azimuthal sectors. The support structure also provides a common electric ground for the read-out electronics and sensors. It also conducts heat from the front-end boards to the cooling system. Each of the six detector sectors is cooled by water flowing through a 5 m long aluminum pipe with 6 mm outer diameter and 1 mm thick walls as shown in Fig. 17. With a water flow of 1 l/min per sector and the output-input temperature difference of $\approx 2^{\circ}$C enough cooling is provided to extract $\approx$ 130 W of heat from each of the sectors. With this arrangement, the temperature of FPGAs is maintained at around 40°C (Fig. 18).

On the inside of the outer wall of the ARICH vessel, 18 planar mirrors are mounted to reflect the photons that would otherwise be lost back to the photo-sensitive area (Fig. 5), as discussed in Sec. 2. The mirrors are 13.1 cm wide and 37.3 cm long, with a reflectivity exceeding 85% in the wavelength interval between 250 nm and 600 nm. The front surface technology

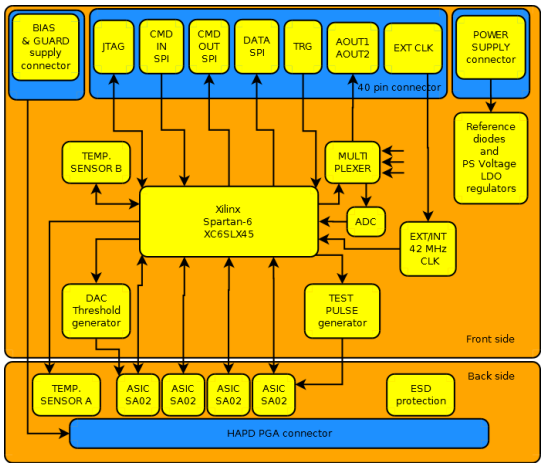

Figure 15: Functional schematic of the front-end board [28] with four custom ASICs on the HAPD side, and a Xilinx Spartan-6 FPGA on the other side of the board.

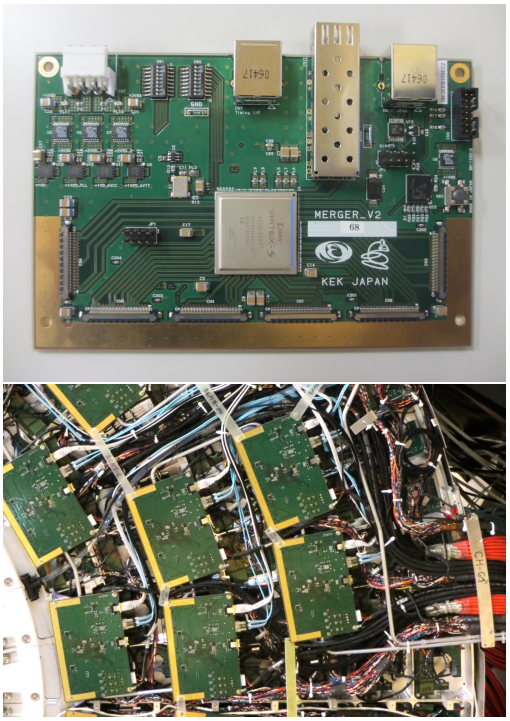

Figure 16: Readout electronics: merger board (top) and mounted merger boards with services (bottom).

is used to reflect photons from the surface coating, to prevent the emission of additional Cherenkov photons in the glass.

7. Construction

7.1. Quality assurance of the components

All ARICH components underwent several quality assessment (QA) measurements before the assembly. The operational parameters of the photo sensors were determined, such as high voltage and APD bias voltages, together with measurements of leakage currents, quantum efficiency and a performance test in a magnetic field. Voltages and currents on the front-end electronics were monitored and the response of each channel was tested. Currents through high voltage distribution boards were measured with an applied voltage of 9 kV. If all components reached a satisfactory quality and response, the final module, consisting of an HAPD, a front-end board and a high voltage distribution board (Fig. 13), was assembled and re-tested.

We scanned the sensor surface over the channel centers and measured its response to short, low-intensity laser pulses at different discriminator values (Fig. 19). From this measurement, the gain of individual channels can be extracted. We anticipate the gain will slowly decrease during operation due to irradiation, requiring adjustments to the front-end board ASIC gain and shaping time to compensate.

We also measured and monitored the refractive indices of aerogel tiles and their transmission lengths (Figs. 7, 8, 9).

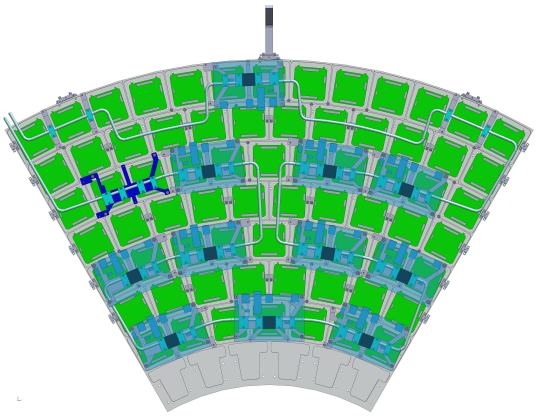

Figure 17: Cooling system of the read-out electronics: cooling pipes are in thermal contact with the merger support elements (dark blue) that are in thermal contact with FPGAs (black squares) on the merger boards (transparent blue), merger board ground-plane, and the main aluminum support structure (in grey). The cooling of the FE boards (in green) is provided through the thermal contact with the main aluminum structure. One of the merger boards has been removed so that the associated support element can be seen (in dark blue); for other mergers, the PCB is shown as transparent so that the FPGAs are visible in black and the connectors in blue.

7.2. Construction

During the quality assurance of the photosensors we observed a position dependence of the quantum efficiency of the photo sensors as displayed in Fig. 12. The variation is significant, since the production specification required only the minimal quantum efficiency value. To equalize the ARICH detector performance across the full active surface, we randomly selected the mounting positions of the HAPDs.

Since the measurements of the properties of aerogel tiles showed minimal variations, the tiles were randomly distributed in the mounting frame during installation.

The ARICH detector is comprised of two halves, one with aerogel tiles and the other with photodetectors and read-out electronics (Fig. 6). Photodetector modules are mounted to the aluminum structure of one of the two halves; they are centered using conical screws, and tightened at the same level with a torque screwdriver. The aerogel tiles are fixed to the structure

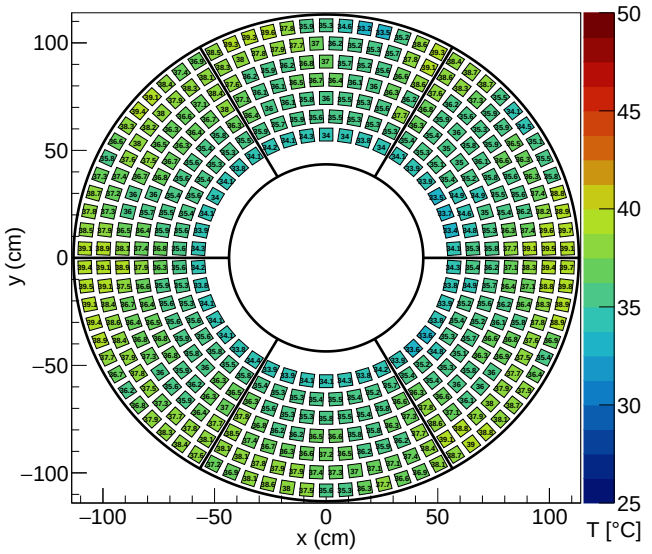

Figure 18: Temperature of the front-end boards during regular data taking operation.

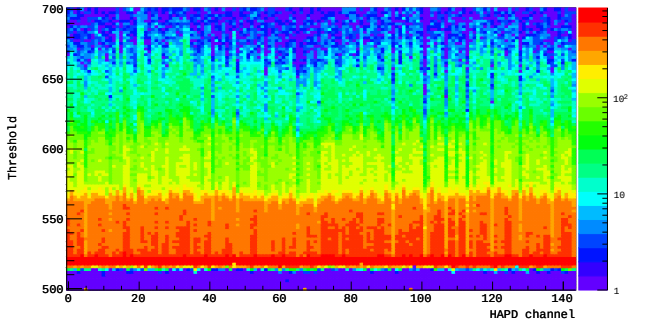

Figure 19: Threshold scan of the 144 channels of a HAPD: the responses of pads illuminated by short laser light pulses at different threshold voltages.

of the other ARICH half with very thin carbon fiber strings to keep them in place when the vector is in the vertical position. Eighteen planar mirrors were installed at the sides of the detector plane.

The sensor and aerogel planes were combined, and aluminum panels were attached at the edges, as seen in Fig. 20. The cables for power supply and data transfer were custom-made primarily on-site.

8. Slow control system

The Belle II ARICH slow control system [30] comprises four subsystems. The High Voltage System controls and monitors the HAPD high voltages, the Low Voltage Control System manages the voltage supplies to the readout electronics, the Environmental Monitor monitors the detector temperature, and the Front-End Board Control System uploads firmware, sets parameters of the readout chip, controls temperature, and manages the single event upset mitigation controller [29].

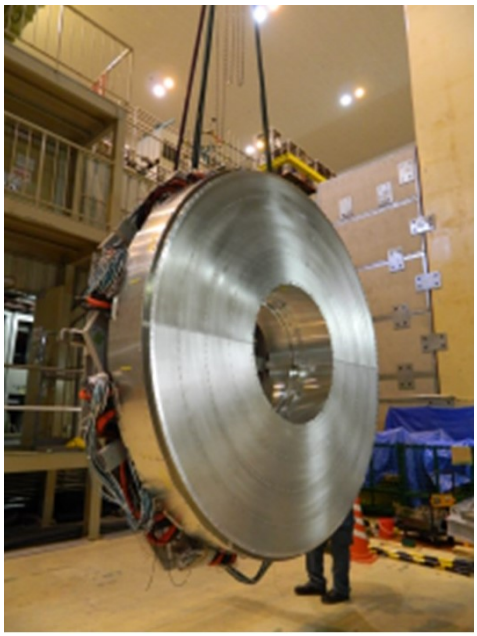

Figure 20: ARICH detector construction: combining the two detector halves.

The control daemons communicate with other processes using the common Belle II Belle2Link [27] and the Network Shared Memory 2 (NSM2) protocol. They accept requests to enable and disable supply channels and adjust hardware settings. Configuration settings are loaded from a common Belle II database, allowing for flexible and controlled value changes. The slow control system also continuously monitors voltage, current, and other detector parameters, such as temperatures and the number of hits. The values of the monitored parameters are regularly stored in the EPICS Archiver Appliance of the Belle II experiment [31], and only significant changes from previous readings are saved. This approach reduces the need to store large amounts of data from more than 15,000 monitoring variables. The slow control graphical user interfaces implemented in Control System Studio [32, 33] visualise the current status and history of the slow control variables in an organised manner (Fig. 21). Finally we note that a special tool was developed with a graphical interface which visualises the connections between different detector parts. This feature was crucial during the installation and commissioning phases and also during the operation for identifying malfunctioning parts.

8.1. High Voltage and Low Voltage Systems

The high voltage (HV) system is controlled by HV daemons that communicate with the hardware using the CAEN HV wrapper library. To minimize discharge risks, all 6 HV channels supplying a given HAPD are synchronous and follow well-defined transitions between different system states. Hardware interlocks ensure safe operation. Over 10,000 parameters are read from the high-voltage boards every ten seconds and recorded in the archiver database. For instance, the history of bias currents helps estimate background irradiation levels on different detector parts (Fig. 22).

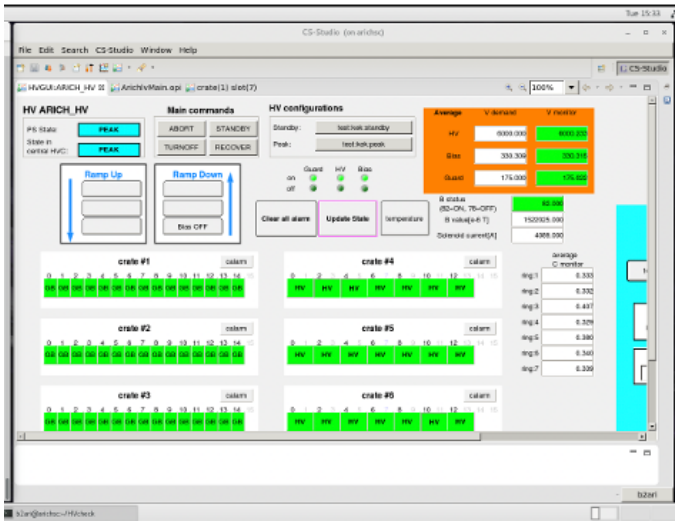

Figure 21: The main graphical user interface for slow control **a better version needed**.

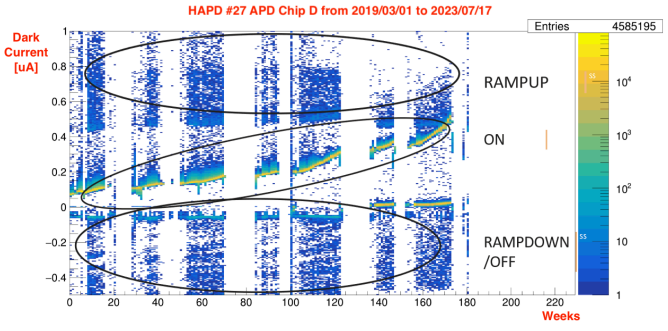

Figure 22: Dark current of one of the APD chips, shown as a function of time. **a better version needed**

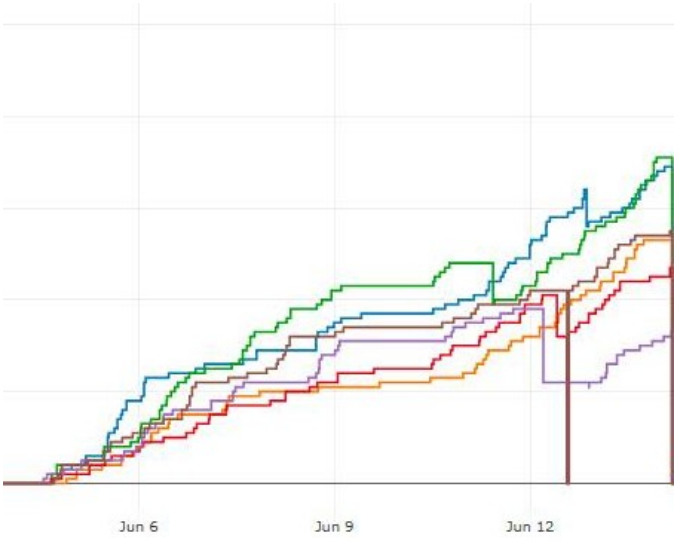

Figure 23: Cumulative number of single event upsets in the front end board FPGAs shown for each of the sectors as a function of time, for one of the data-taking periods. **needs a better version, possibly to be replaced by a plot of SEU rate v.s. TOP hit rate**

The low-voltage supply slow control system is controlled by a separate deamon that communicates with the Wiener MPOD crate controller using the Simple Network Management Protocol (SNMP). In the same manner as the high voltage deamon, it ensures that the groups of voltages supplying a group of HAPD baseboards and merger boards are switch together.

8.2. Data quality monitors

Additional processes continuously extract key parameters from the reconstruction running online on a fraction of the data. These parameters include the Cherenkov angle of high momentum tracks, the number of hits per track, the numbers of hot and dead channels, and the temporal distribution of hits. The temporal changes of these parameters are monitored via various web interfaces (Figs. 25 and 28).

8.3. Environmental monitors

The data acquisition controller implements a process that controls the parameter settings of the readout cards and monitors their basic functionality, including readings of supply voltages, temperatures, and single-event upset (SEU) counts (Figs. 18 and 23). Additionally, it monitors the temperature of inlet and outlet water cooling pipes and the status of the cooling unit. Additional temperature sensors at various parts of the detector are read from a common Belle II environmental monitoring system.

9. Commissioning and Operation

9.1. Commissioning

The ARICH detector commissioning phase started early in 2018, together with the commissioning of all other components

of the Belle II spectrometer. During this phase, the detector quickly turned out to operate reliably.

Before the start of data acquisition, the front-end boards had to be programmed to set for each ASIC a common gain, discrimination threshold, and channel-dependent offsets. An example of a calibration of the channel offsets is shown in Fig. 24. Offsets calculated from the upper plot were uploaded to the detector, allowing one common threshold to discriminate between hit and non-hit channels. Offsets calculated from the upper plot

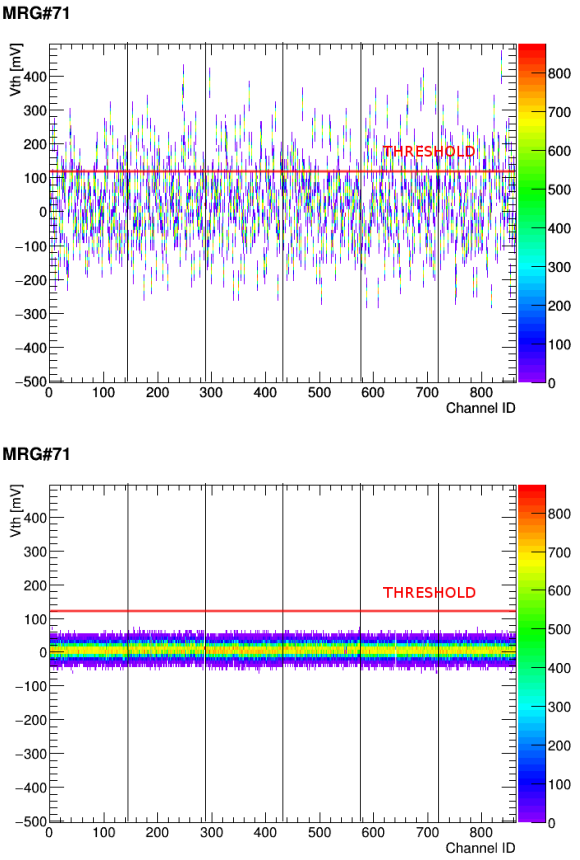

Figure 24: Response of the detector, a threshold scan for each of the channels of a single merger board with six front-end boards connected (corresponding to $6 \times 144 = 864$ channels). Upper plot: non-calibrated offsets, lower plot: threshold scan with calibrated offsets.

were uploaded to the detector, allowing one common threshold to discriminate between hit and non-hit channels.

The initial commissioning showed that the cooling system required an upgrade to boost its performance by a more efficient thermal coupling to the read-out electronics boards to the cooling system. This upgrade was carried out during the summer shutdown in 2018. By the end of 2018, the commissioning phase was completed, and was followed by the first physics data-taking runs in the spring of 2019.

9.2. Operation

The ARICH detector turned out to run stably from the commissioning phase on. As already discussed above, various parameters are continuously monitored to ensure a stable performance in react in case of deviations in performance.

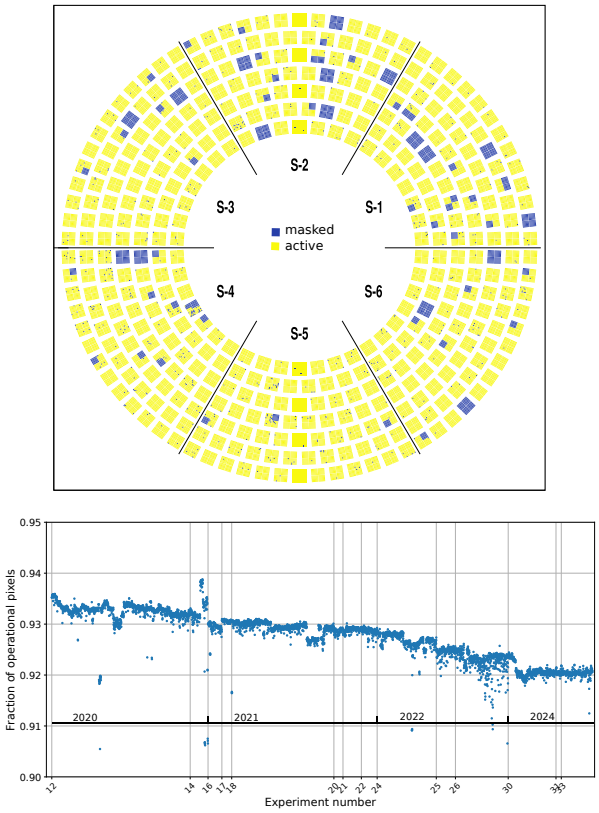

Figure 25: Masked channels: distribution over the photon detector at the beginning of Run 2 in December 2023 (top); variation of the number of masked channels with time (bottom).

To monitor the performance of the photo-sensors, LED light ($\lambda = 470$ nm) emitted from LEDs and distributed through optical fibers to 90 points in the gaps between the photo sensors is used on a regular basis. The light is reflected from the aerogel surface and is spread over the surface covered by HAPDs; it is used to identify noisy and dead channels, as well as for measuring the relative sensitivity and gain of each channel.

During the acquisition of beam collision data, the quality of the data is constantly monitored. In the event-based filter, HAPD sensors with too many hits are rejected. Checks of dead and noisy channels (Figs. 25 and 26) is carried out for each run, and new channels that appear in this list are taken into account in the reconstruction.

As discussed in Sec. 5, the hit information is read out in four adjacent 125.6 ns long time intervals, where the middle two are adjusted to the correct timing with respect to the L1 trigger, and the two side bins are used to estimate the background level on an event-by-event basis (Fig. 27).

We also monitor the overall performance of the detector by checking the two most relevant variables, the Cherenkov angle and the number of detected Cherenkov photons of ultra-relativistic muon tracks ($p > 4$ GeV/c). As shown in Fig. 28, the detector indeed performs reliably over extended periods of time.

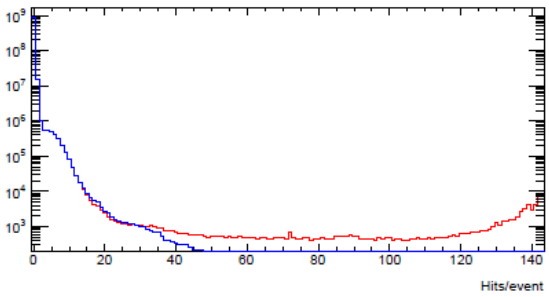

Figure 26: Number of hits per sensor per event. All sensor hits (red) and accepted hits (blue).

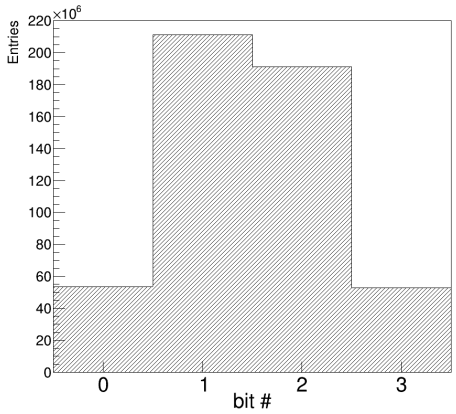

Figure 27: Timing alignment of hits: central two bins correspond to hits in the signal windows, while the left and right bins correspond to off-time background hits.

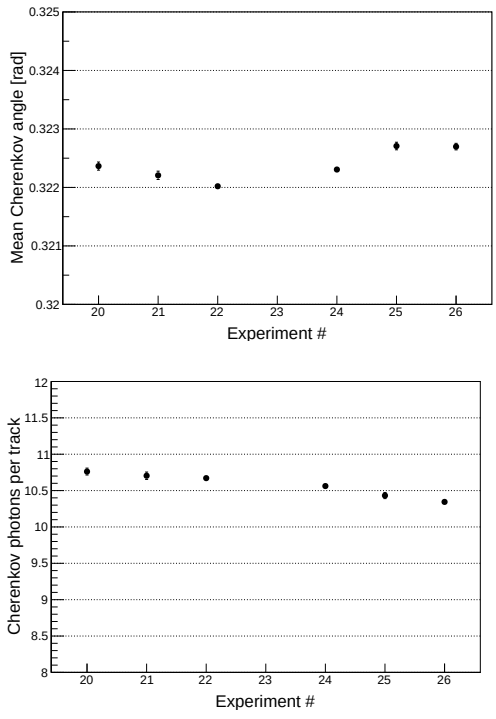

Figure 28: Detector performance as a function of time: Cherenkov angle (top) and number of photons (bottom) for ultra-relativistic muon tracks ($p >$ 4 GeV/c). **the plot of the number of photons to be replaced by a better version (with a refined acceptance correction?)**

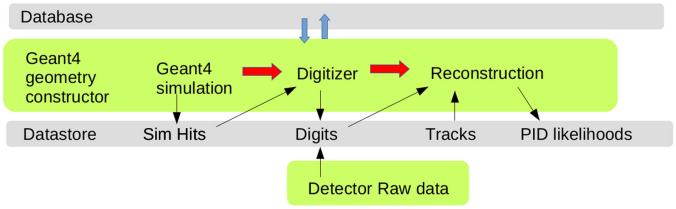

Figure 29: ARICH software scheme.

10. Simulation and reconstruction

The ARICH simulation and reconstruction software is integrated into Basf2 (Belle Analysis Software Framework 2) [34] which provides a common framework for the Belle II detector simulation, event reconstruction, and data analysis. The code is organized in the form of independent modules (mostly written in C++) that perform a specific task and are included in the main event processing loop using Python-based steering files. For the ARICH detector the basic structure of the event loop is shown in Figure 29. For the simulated data the loop starts with the Geant4 simulation of the event. In the simulation, photon hits on the photon detectors are recorded. At the stage of digitization, these hits are converted to the so-called digits, which correspond to the actual output from the detector (i.e., containing only hit channel numbers). For the analysis of measured data, the event loop starts with the collection of digits, obtained directly from the raw data. Finally, the ARICH reconstruction module uses the collection of tracks impacting on the aerogel (obtained from the Belle II tracking system) and the collection of photon hits to calculate the PID likelihoods for each track.

10.1. Geant4 simulation

The geometry of the ARICH detector is implemented in detail in the Geant4. This includes all the main components relevant to the emission, propagation, and detection of Cherenkov photons, as well as the detector support structures, cooling system, and neutron shielding and cabling material. Since the detector geometry is described elsewhere we only address here items particular to the simulation, which are also relevant in the context of comparing the measured and simulated data.

Aerogel plane. In the simulation, all aerogel tiles of one layer have equal optical properties and thickness. The refractive indices of 1.045 and 1.055, and transmission lengths of 45 mm and 35 mm, are used for all the tiles in the up-stream and down-stream layers respectively (the values given are at 400 nm, but their full wavelength dependency as measured in the QA tests is implemented in the simulation, ref?). Tiles are of four different ”wedge” shapes (different in each concentric ring of tiles) and have a uniform thickness of 20 mm. Tiles are placed at the center of tile slots which are formed by aluminum strips with 1 mm of thickness, with an additional 1 mm of gap between the tile edge and aluminum, on all four sides of a tile (in total, there is therefore a 3 mm of gap between the edges of aerogel tiles). The black paper that covers the tile slots is, for the sake of simplicity, not included in the simulation, but its effect of

photon absorption is mimicked by non-specified optical properties of the aluminum, which results in optical photons being killed upon hitting it.

Photon detector - HAPD. In the simulation, we build the photon detector module as a ceramic box, with the quartz window on the top, the vacuum inside, and the silicon APD chip at the bottom. The dependency of the quartz refractive index on the wavelength is implemented by using data found in the literature. The emission of photo-electrons from the photo-cathode and their propagation to the APDs is not included in the simulation. Instead, for the optical photons that hit the bottom surface of the quartz window, onto which the photo-cathode is coated, the quantum efficiency curve is applied (we randomly select a number from 0 to 1 and compare it with Q.E. at the given photon wavelength). If the photon is registered as detected, it is killed and its position is passed to the so-called digitizer for the next steps of processing (as described in the next subsection). On the other hand, if the photon is not detected, it is left to propagate further, either by being internally reflected in the quartz window or by entering into the HAPD where it can be then reflected from the APD back to the photo-cathode or absorbed. The reflectivity of the APD surface in the simulation is wavelength-independent and is tuned so that the fraction of reflected photons agrees with the one observed in the measured data. At this point, the same Q.E. curve is used for all HAPDs, which is corrected to the exact values during the digitisation step (see below).

Other components. Here we give a few relevant comments on other detector components. The mirrors are implemented as quartz planes coated with a reflective metal, where the reflectivity and its wavelength dependency are set to the values as obtained in QA measurements. The front-end electronics (HAPD front-end boards and merger boards) are implemented as simple boxes, of correct dimensions, made of material commonly used for effective description of PCBs. The geometry of cooling bodies (behind each FEB and merger board) and cooling pipes is implemented in fine details. On the other hand, the detector cabling (HV, LV, read out) is included by placing a simple homogeneous thin plane with the amount and type of material that effectively describes the cabling material, behind the photon-detector plane. Finally, the borated polyethylene neutron shield volumes are also included, with precisely described shapes and sizes.

Since the peak Q.E. of HAPDs is $\sim 40\%$, only this fraction of emitted optical photons is actually propagated in the simulation, while the rest are killed immediately at the emission time. This allows to speed up the detector simulation without affecting its output.

10.2. Digitization

In the digitizer module the photon hits obtained from the Geant4 are converted into the data format equivalent to the one of the measured data (i.e. the collection of channel numbers of hit APD pixels). There are four processes that are done at this stage:

- Pixelization: based on the registered photon hit position we calculate the pixel number to which this position corresponds. Here we assume that the emitted photo-electron only moves in the z direction, i.e. along the magnetic field lines.

- Channel-by-channel Q.E. correction: at the simulation level a common wavelength dependence of Q.E. is used for all HAPDs. However, since relatively large differences in the Q.E. are observed between individual samples, and the Q.E. non-uniformity over the surface of individual sensors cannot be neglected, we apply a channel-by-channel Q.E. correction, using the measured Q.E. surface maps of individual HAPDs.

- Dead channel masking: about 5% of channels are non-operational; we keep the list of these channels in the data base and use it for the production of simulated data.

- Effect of negative polarity cross-talk: if a single pixel is hit by a large number of photo-electrons, the efficiency of neighbouring pixels to detect photo-electron is reduced. This effect is included in the digitizer where we count the number of photo-electrons on each pixel and proportionally to it lower the efficiency of the neighbouring pixels.

The list of so-called digits, which contain the photon-detector module ID number, channel ID number, and a hit bitmap[4] is the final output of the Geant4 simulation.

The simulation of ARICH detector response is checked by high momentum muon tracks from the $e^+e^- \to \mu^+\mu^-$ events, comparing the Cherenkov ring image in measured and simulated events. The top two plots of Fig. 30 show the reconstructed Cherenkov ring image in the angular coordinate system of a track[5] for the measured and simulated data. The image is obtained as a normalized sum of Cherenkov rings from $O(10\text{k})$ muon tracks. Several detailed features, such as Cherenkov photons produced in the quartz window of photon detectors and an "echo ring" originating from the non- converted photons reflected from the APD surface back to the photo-cathode, can be seen to be well reproduced in the simulation. Some discrepancies between the measured and simulated data can be seen in the peak produced by charged tracks in the window of photon detectors at small Cherenkov angles. This arises due to the difficulty of correctly modeling the optical properties of the photo-cathode and the response of the avalanche photo-diode to a large number of photons. Based on these observations mentioned effects will be adjusted for in the detector simulation.

10.3. Event reconstruction

Reconstructed tracks from the Belle II tracking system are extrapolated to the ARICH detector volume and for the ones

[4] These are four time-consecutive bits, which indicate whether the signal exceeded the threshold value in a given time bin or not.

[5] In this system the track direction corresponds to (0,0) and the distance from the origin shows the photon direction polar angle, i.e. Cherenkov angle.

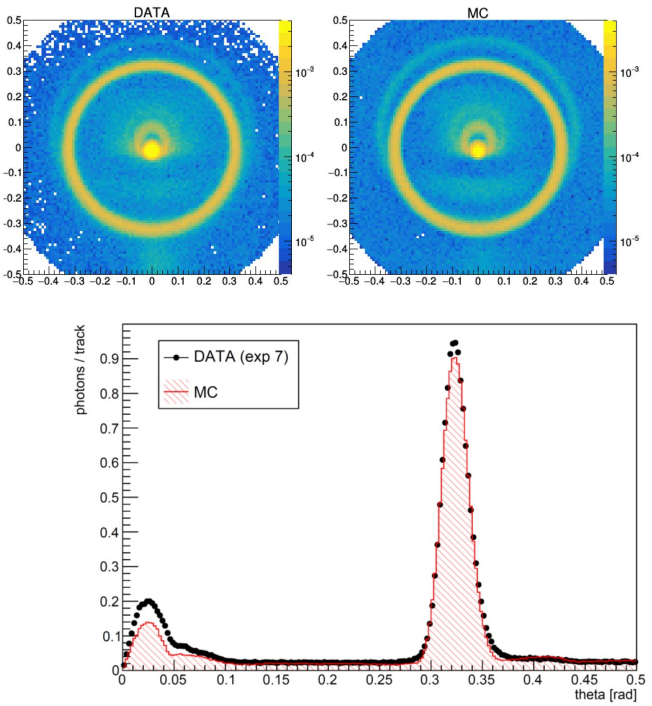

Figure 30: Calibration of the simulated detector response; top: comparison of accumulated Cherenkov ring images as observed in the measured data and the detector simulation; bottom: comparison of measured and simulated Cherenkov angle distributions (integral of top two plots over the ring azimuthal angle).

that pass through the aerogel layer a likelihood function is constructed for each of the six different particle type hypotheses (e, μ, π, K, p, d). The likelihood function compares the observed pattern of photon hits with the expected one for the given particle type hypothesis and track parameters (position, direction and momentum on the aerogel plane) as obtained from the track extrapolation.

The likelihood function is constructed as a product of probabilities of individual pixels recording the observed number of hits (which can only be 0 or 1 since we do not discriminate between single and multiple photon hits) for a given particle type hypothesis. The probability of pixel i being hit by m_i photo-electrons is given by the Poissonian distribution, i.e., $p_i = e^{-n_i} n_i^{m_i}/m_i!$, where n_i is the number of photo-electrons expected to hit the pixel i. The value of n_i is a sum of the expected number of hits from two radiator layers and from the background. The contribution of each radiator to the signal on the individual pixel is calculated according to the probability distribution in the polar and azimuthal angles relative to the track direction over the solid angle subtended by the pixel i; the method is discussed in detail in [35].

Following P. Baillon [36] and R. Forty [37] to construct the likelihood function, we first note that the probability of a pixel being fired or not is $1 - e^{-n_i}$ and e^{-n_i}, respectively, and the logarithm of the likelihood function is

$$\ln \mathcal{L} = \sum_{hit} \ln\left(1 - e^{-n_i}\right) + \sum_{no\ hit} \ln\left(e^{-n_i}\right)$$
$$= \sum_{hit} \left[n_i + \ln\left(1 - e^{-n_i}\right)\right] - \sum_{all} n_i = \sum_{hit} \ln\left(e^{n_i} - 1\right) - N,$$

where *hit* / *no hit* / *all* indicates the subset of pixels included in the sum, and we note that the sum of n_i over all pixels is equal to the total number of photons expected to be detected (denoted by N). Instead of having to obtain n_i for all pixels, in this form evaluating the likelihood reduces to the calculation of n_i only for pixels that registered a hit, and to the estimation of N. Both n_i and N have to be evaluated for each particle type hypothesis. Finally, the difference of likelihoods of two hypotheses (e.g. $\ln \mathcal{L}^\pi - \ln \mathcal{L}^K$) is used for separation between particle species (π, K).

10.4. Calibration and alignment

Calibrating the detector is essential due to its significant impact on algorithm performance. Calibration affects the expected number of photons per pixel (n_i) in the likelihood function, incorporating both background and signal contributions. The signal component relies on the detection efficiency of the pad (η_i) and the probability density function determined by the Cherenkov angle resolution (σ_θ). Without proper calibration, identification efficiencies decrease and misidentification probabilities increase.

The detector response and alignment with the tracking system were calibrated using recorded data, primarily from $e^+e^- \to \mu^+\mu^-$ events [35, 38]. This calibration process involved several steps. First, the operational parameters of the detector components were measured. Next, the detector was calibrated using the acquired data. Finally, the crucial step for subsequent physics analyses was determining the efficiencies and misidentification probabilities from beam collision data.

The reconstruction algorithms could access all the measured and calculated parameters in a central experiment database.

Cherenkov angle distribution for saturated rings is used to calculate the number of detected photons per track. With the procedure described above, the detection efficiency of each hit, η_i, and the total number of photons per hypothesis, N, can then be calculated.

To complete the calibration, the Cherenkov angle resolution, σ_θ, must be optimized by aligning the detector [38]. From displacements at different positions of the detector, new alignment constants are determined, leading to the correct σ_θ, which can then be used in the algorithm.

11. Particle identification performance

The ARICH detector has been running stably throughout all running periods of the Belle II experiment. The fraction of dead or noisy channels has been at the 5% level; as determined from simulation, such a level of missing channels is by a large margin below the level that would impact the particle identification performance of the device.

The performance of the detector was first checked by a large number of available muon tracks originating from the $e^+e^- \to \mu^+\mu^-$ events. Muons from these events have the energy of about 7 GeV, producing essentially saturated Cherenkov rings in the ARICH. From the bottom plot of Fig. 30 we determine the number of signal Cherenkov photons and the Cherenkov angle resolution for measured data and simulation by fitting the obtained distributions with a single Gaussian function for the peak and a first-order polynomial for the background distribution. The obtained numbers of signal photons per muon track are $N_{sig}^{data} = 11.38$ and $N_{sig}^{MC} = 11.27$ for the measured and simulated data respectively, while the corresponding Cherenkov angle resolutions (i.e. signal peak width) are $\sigma_c^{data} = 12.70$ mrad and $\sigma_c^{MC} = 12.75$ mrad (with negligible uncertainties from the fit).

We estimate the detector ability to discriminate between pions and kaons using pion and kaon tracks from $D^{*+} \to D^0[\to K^-\pi^+]\ \pi^+_{\rm slow}$ and $D^{*-} \to \bar{D}^0[\to K^+\pi^-]\ \pi^-_{\rm slow}$ decay chains. Here, pion and kaon tracks can be identified independently of ARICH information, based on their charge in association with the charge of low momentum pion ($\pi^\pm_{\rm slow}$) from $D^{*\pm}$. In addition, the background level in this decay mode can be effectively reduced by requiring the difference of reconstructed invariant masses of D^* and D^0 mesons to be within a narrow window around the expected value ($|M_{D^*} - M_{D^0} - 145.43\ {\rm MeV}/c^2| < 1.5\ {\rm MeV}/c^2$ is used). We determine the efficiency of kaon identification and pion misidentification probability from the signal yield of reconstructed D^0 mesons, where pion or kaon track used in the reconstruction is required to satisfy the imposed selection criteria on PID likelihood ratio $R[K/\pi]$ obtained from the ARICH detector, with $R[K/\pi] = \mathcal{L}_K/(\mathcal{L}_K + \mathcal{L}_\pi)$. The D^0 signal yield is determined from the fit of D^0 invariant mass distribution using a Gaussian function for the signal and a constant value for the background distributions. An example of such a fit is shown in the top two plots of figure 31. Left (right) plot shows data distribution and fit of D^0 invariant mass for candidates with pion (kaon) track entering ARICH. Fainted points and lines show the case when no selection is imposed on $R[K/\pi]$ and solid points and lines after imposing a $R[K/\pi]$ requirement. Repeating such fit using different $R[K/\pi]$ criteria results in the bottom left plot of figure 31, which shows the obtained kaon identification efficiency at different pion misidentification probabilities. The right bottom plot shows the dependence of these two quantities on the track momentum, where a fixed criterium of $R[K/\pi] > 0.5$ is used at all points. The obtained performance is slightly lower than expected from the simulations (up to a few % in K identification efficiency), further improvements are under study. We note that the ARICH detector also provides excellent pion-proton and kaon-proton discrimination, and at momenta below 1 GeV/c a modest discrimination between pions, muons and electrons; hadron identification performance of all involved subsystems in the Belle II spectrometer is discussed in detail in a dedicated report [39].

12. Summary

The Aerogel RICH detector in the forward end-cap of the Belle II spectrometer is an integral part of the Belle II particle identification system. It is based on a novel multi-layer radiator configuration and uses a new type of single photo sensor, hybrid avalanche photodetectors (HAPD). It provides excellent discrimination between pions and kaons in the full kinematic range of the experiment (up to 4 GeV/c). The detector has been performing very well throughout the Belle II data-taking and is expected to continue contributing to the future physics harvest of the experiment.

13. Acknowledgements

We thank the SuperKEKB group for the excellent operation of the accelerator; the KEK cryogenics group for the efficient operation of the solenoid; the KEK computer group for on-site computing support; and the raw-data centers at BNL, DESY, GridKa, IN2P3, and INFN for off-site computing support.

This work was supported by the following funding sources: European Research Council, Horizon 2020 ERC-Advanced Grant No. 884719; Slovenian Research Agency research grants No. J1-9124, J1-4358 and P1-0135; Higher Education and Science Committee of the Republic of Armenia Grant No. 23LCG-1C011; **Japanese funding details to be added**.

References

[1] Yukiyoshi Ohnishi et al. Accelerator design at SuperKEKB. *PTEP*, 2013:03A011, 2013.

[2] T. Abe et al. Belle II Technical Design Report. 11 2010.

[3] I. Adachi, T. E. Browder, P. Križan, S. Tanaka, and Y. Ushiroda. Detectors for extreme luminosity: Belle II. *Nucl. Instrum. Meth. A*, 907:46–59, 2018.

[4] I. Adachi et al. The Belle II Detector at the SuperKEKB Flavor Factory. *to be submitted to JINST*, 2024.

[5] H. Atmacan et al. The imaging Time-of-Propagation detector at Belle II. *Nucl. Instrum. Meth. A*, 1080:170627, 2025.

[6] T. Matsumoto et al. Studies of proximity focusing RICH with an aerogel radiator using flat panel multianode PMTs (Hamamatsu H8500). *Nucl. Instrum. Meth. A*, 521:367–377, 2004.

[7] T. Iijima, S. Korpar, et al. A novel type of proximity focusing RICH counter with multiple refractive index aerogel radiator. *Nucl. Instrum. Meth. A*, 548:383–390, 2005.

[8] Peter Križan, Samo Korpar, and Toru Iijima. Study of a nonhomogeneous aerogel radiator in a proximity focusing RICH detector. *Nucl. Instrum. Meth. A*, 565:457–462, 2006.

[9] P. Križan et al. Aerogel rich, January 2004. presented at the Super B Factory Workshop, Honolulu, Hawaii, http://www.phys.hawaii.edu/superb04.

[10] A.Yu. Barnyakov, M.Yu. Barnyakov, V.S. Bobrovnikov, A.R. Buzykaev, A.F. Danilyuk, V.L. Kirillov, S.A. Kononov, E.A. Kravchenko, and A.P. Onuchin. Focusing aerogel rich (farich). *Nuclear Instruments and Methods in Physics Research Section A: Accelerators, Spectrometers, Detectors and Associated Equipment*, 553(1-2):70 – 75, 2005. Proceedings of the fifth International Workshop on Ring Imaging Detectors.

[11] I. Adachi, S. Fratina, T. Fukushima, A. Gorisek, T. Iijima, H. Kawai, M. Konishi, S. Korpar, Y. Kozakai, P. Križan, T. Matsumoto, Y. Mazuka, S. Nishida, S. Ogawa, S. Ohtake, R. Pestotnik, S. Saitoh, T. Seki, T. Sumiyoshi, M. Tabata, Y. Uchida, Y. Unno, and S. Yamamoto. Study of highly transparent silica aerogel as a rich radiator. *Nuclear Instruments and Methods in Physics Research Section A: Accelerators, Spectrometers, Detectors and Associated Equipment*, 553(1-2):146 – 151, 2005. Proceedings of the fifth International Workshop on Ring Imaging Detectors.

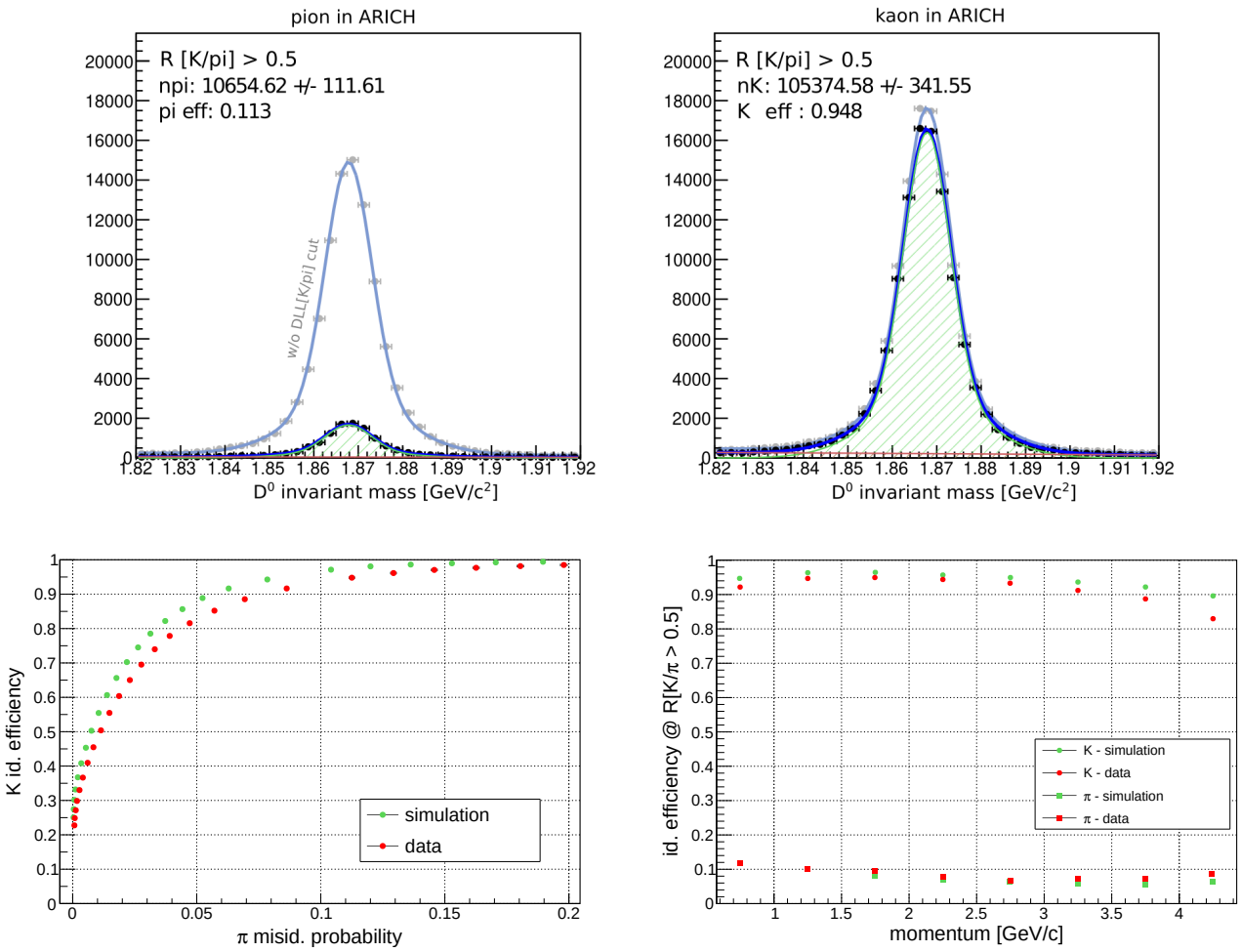

Figure 31: ARICH detector, performance. Top: examples of fits of the $K^{\mp}\pi^{\pm}$ invariant mass distributions from which we determine kaon identification efficiency and pion misidentification probability at a given criterion on $R[K/\pi]$. Bottom left: kaon identification efficiency versus pion misidentification probability for all kaon/pion tracks from D^0 decays that enter the ARICH detector; right: kaon identification efficiency and pion misidentification probability as a function of track momentum for a fixed likelihood ratio, $R[K/\pi] > 0.5$.

[12] S. Korpar et al. Proximity focusing RICH with TOF capabilities. In *2006 IEEE Nuclear Science Symposium and Medical Imaging Conference and 15th International Room Temperature Semiconductor Detector Workshop*, 5 2007.

[13] S. Korpar, P. Križan, and Rok Pestotnik. Timing and cross-talk properties of BURLE multi-channel MCP PMTs. *PoS*, PD07:021, 2006.

[14] P. Križan et al. Tests of the Burle 85011 64-anode MCP PMT as a detector of Cherenkov photons. *Nucl. Instrum. Meth.*, A567:124–128, 2006.

[15] M. Akatsu et al. MCP-PMT timing property for single photons. *Nucl. Instrum. Meth.*, A528:763–775, 2004.

[16] S. Korpar et al. Proximity focusing RICH with TOF capabilities. *Nucl. Instrum. Meth.*, A572:432–433, 2007.

[17] S. Korpar, R. Dolenec, K. Hara, T. Iijima, P. Križan, Y. Mazuka, R. Pestotnik, A. Stanovnik, and M. Yamaoka. Measurement of Cherenkov photons with silicon photomultipliers. *Nucl. Instrum. Meth. A*, 594:13–17, 2008.

[18] Samo Korpar, Hassan Chagani, Rok Dolenec, Peter Križan, Rok Pestotnik, and Ales Stanovnik. A module of silicon photo-multipliers for detection of Cherenkov radiation. *Nucl. Instrum. Meth. A*, 613:195–199, 2010.

[19] I. Adachi et al. Construction of silica aerogel radiator system for Belle II RICH Counter. *Nucl. Instrum. Meth. A*, 876:129–132, 2017.

[20] S. Nishida et al. Development of a 144-channel Hybrid Avalanche Photo-Detector for Belle II ring-imaging Cherenkov counter with an aerogel radiator. *Nucl. Instrum. Meth. A*, 787:59–63, 2015.

[21] S. Korpar et al. A 144-channel HAPD for the Aerogel RICH at Belle II. *Nucl. Instrum. Meth. A*, 766:145–147, 2014.

[22] Shohei Nishida, Ichiro Adachi, Toru Iijima, Hirokazu Ikeda, Samo Korpar, Peter Križan, Yuichi Miyazawa, Isao Nishizawa, and Takayuki Sumiyoshi. Development of an HAPD with 144 channels for the aerogel RICH of the Belle upgrade. *Nucl. Instrum. Meth. A*, 595:150–153, 2008.

[23] S. Nishida et al. Aerogel RICH for the Belle II forward PID. *Nucl. Instrum. Meth. A*, 766:28–31, 2014.

[24] L. Šantelj et al. Studies of a hybrid avalanche photo-detector in magnetic field. *Nucl. Instrum. Meth. A*, 845:459–462, 2017.

[25] S. Nishida et al. Readout ASICs and Electronics for the 144-channel HAPDs for the Aerogel RICH at Belle II. *Phys. Procedia*, 37:1730–1735, 2012.

[26] A. Seljak et al. Readout electronics for a Hybrid Avalanche Photon Detector. *JINST*, 6:C12051, 2011.

[27] Dehui Sun et al. Belle2Link: A Global Data Readout and Transmission for Belle II Experiment at KEK. *Physics Procedia*, 37:1933–1939, 2012.

[28] R. Pestotnik et al. Front-end electronics of the Belle II aerogel ring imaging detector. *Nucl. Instrum. Meth. A*, 952:161711, 2020.

[29] R. Giordano, Y. Lai, S. Korpar, R. Pestotnik, A. Lozar, L. Šantelj, M. Shoji, and S. Nishida. Frame-level intermodular configuration scrubbing of on-detector fpgas for the arich at belle ii. *IEEE Transactions on Nuclear Science*, 68(12):2810–2817, 2021.

[30] R. Pestotnik et al. Slow control of the Belle II Aerogel Ring Imaging detector. *Nucl. Instrum. Meth. A*, 1056:168569, 2023.
[31] Murali Shankar, Luofeng Li, and Martin Konrad. The epics archiver appliance. 10 2015.
[32] M. R. Clausen, C. H. Gerke, M. Moeller, H. R. Rickens, and J. Hatje. Control system studio (CSS). In *Proceedings of ICALEPCS'07*, Oak Ridge, TN, USA, October 2007.
[33] Experimental_Online_and_Control. Control system studio. `https://control-system-studio.org/`, 2024. Accessed: 2024-07-18.
[34] L. Šantelj et al. Recent developments in software for the Belle II aerogel RICH. *Nucl. Instrum. Meth. A*, 876:104–107, 2017.
[35] R. Pestotnik et al. Calibration of the Belle II aerogel ring imaging detector. *Nucl. Instrum. Meth. A*, 952:161800, 2020.
[36] P. Baillon. Cherenkov ring search using a maximum likelihood technique. *Nucl. Instrum. Meth. A*, 238:341, 1985.
[37] R. Forty. RICH pattern recognition for LHCb. *Nucl. Instrum. Meth. A*, 433:257–261, 1999.
[38] S. Tamechika et al. Development of alignment algorithm for Belle II Aerogel RICH counter. *Nucl. Instrum. Meth. A*, 952:162337, 2020.
[39] I. Adachi et al. Charged-hadron identification at Belle II. 6 2025.